Published in final edited form as:

Proteins. 2016 August ; 84(8): 1162–1172. doi:10.1002/prot.25062.

Structural Analysis of Nested Neutralizing and Non-Neutralizing B cell Epitopes on Ricin Toxin's Enzymatic Subunit

Michael J. Rudolph[1,*], **David J. Vance**[2], **Michael S. Cassidy**[1], **Yinghui Rong**[2], **Charles B. Shoemaker**[4], and **Nicholas J. Mantis**[*,2,3]

[1]New York Structural Biology Center, New York, New York 10027

[2]Division of Infectious Diseases, Wadsworth Center, New York State Department of Health, Albany, NY, 12208

[3]Department of Biomedical Sciences, University at Albany, Albany, NY 12201 United States

[4]Tufts Cummings School of Veterinary Medicine, North Grafton, MA 01536

Abstract

In this report we describe the X-ray crystal structures of two single domain camelid antibodies (V_HH), F5 and F8, each in complex with the ricin toxin's enzymatic subunit (RTA). F5 has potent toxin-neutralizing activity, while F8 has weak neutralizing activity. F5 buried a total of 1760 $Å^2$ in complex with RTA and made contact with three prominent secondary structural elements: α–helix B (residues 98-106), β–strand h (residues 113-117), and the C-terminus of α–helix D (residues 154-156). F8 buried 1103 $Å^2$ in complex with RTA that was centered primarily on β–strand h. As such, the structural epitope of F8 is essentially nested within that of F5. All three of the F5 complementarity determining regions (CDR) were involved in RTA contact, whereas F8 interactions were almost entirely mediated by CDR3, which essentially formed a seventh β–strand within RTA's centrally located β–sheet. A comparison of the two structures reported here to several previously reported (RTA- V_HH) structures identifies putative contact sites on RTA, particularly α–helix B, associated with potent toxin-neutralizing activity. This information has implications for rational design of RTA-based subunit vaccines for biodefense.

Introduction

Ricin is a member of the ribosome-inactivating protein (RIP) family of toxins found throughout the plant and microbial worlds[1,2]. Ricin toxin is present at high concentrations in the beans of the castor oil plant, *Ricinus communis*, which is ubiquitous in tropical and subtropical environments. In its mature form, ricin is a 65 kDa glycoprotein consisting of two subunits, RTA and RTB, joined by a single disulfide bond[3]. RTA (267 amino acids) is an RNA N-glycosidase (EC 3.2.2.22) that selectively inactivates eukaryotic ribosomes through cleavage of a universally conserved ribosomal RNA element known as the sarcin-ricin loop

*To whom correspondence should be addressed: Dr. Michael J. Rudolph, New York Structural Biology Center, 89 Convent Avenue, New York, NY 10027, Tel. 212-939-0660 and address: mrudolph@nysbc.org and Dr. Nicholas J. Mantis, Division of Infectious Disease, Wadsworth Center, New York State Department of Health, 120 New Scotland Ave, Albany, NY 12208. Tel. 518-473-7487. address: nicholas.mantis@health.ny.gov.

(SRL)[4,5]. RTB is a galactose-specific lectin that mediates ricin attachment and entry into mammalian host cells[6]. Following uptake, RTB facilitates retrograde trafficking of ricin to the endoplasmic reticulum. In the endoplasmic reticulum, RTA dissociates from RTB then retrotranslocates into the cytosol where it potently inactivates ribosomal function[7].

There are ongoing efforts to develop a recombinant RTA-based subunit vaccine as a countermeasure against ricin toxin, which is classified as a biothreat agent by the Centers for Disease Control and Prevention. The two vaccines, RiVax™ and RVEc™, were rationally designed based on information gained through X-ray crystallography and site-directed mutagenesis[8-10]. Structurally, RTA consists of three distinct folding domains[11,12]. Folding domain I (residues 1-117) is dominated by a six-stranded β-sheet that terminates in a solvent exposed α-helix, known as α-helix B (residues 97-108). The α-helix B is conserved among the family of RIPs and is a target of several well-characterized toxin-neutralizing monoclonal antibodies (mAbs), including PB10 [13-16]. Folding domain II (residues 118-210) is dominated by five α helices (C-G) that run through the center of RTA, while folding domain III (residues 211-267) forms a protruding element that interacts with RTB [11]. RTA's active site constitutes a shallow pocket in the central portion of the protein. Five residues (i.e., Tyr80, Tyr123, Glu177, Arg180, and Trp211) situated within or near the active site cleft are essential for RTA's enzymatic activity. RiVax is a full-length derivative of RTA with point mutations at position Tyr80 to disrupt RNA N-glycosidase activity and Val76 to perturb a motif involved in vascular leak syndrome [17]. RVEc is a truncated version of RTA that lacks residues 199-267, as well as a small hydrophobic loop in the N-terminus (residues 34-43) [8,18,19]. RVEc (also referred to as RTA1-33/44-198) lacks folding domain III and is only 188 residues in length.

While both RiVax and RVEc are able to stimulate protective immunity to ricin in animal models (mouse and non-human primates), the immune response to ricin is actually quite complex [10,20]. Indeed, there is evidence to suggest that vaccination stimulates a polyclonal antibody response consisting largely of non-neutralizing or poorly neutralizing antibodies [16,20,21]. We have proposed that toxin-neutralizing antibodies constitute only a tiny fraction (1-10%) of the total antibody response to RiVax or RVEc and target a limited number of epitopes within four spatially confined regions referred to as Clusters I-IV [16,22]. Cluster I, for example, is defined by mAb PB10, whose epitope is centered on α-helix B (residues 97-108) [16,22,23]. The results of competition ELISAs suggested that antibodies that compete with PB10 for binding to RTA were invariably associated with toxin-neutralizing activity (TNA), further supporting the notion neutralizing and non-neutralizing antibodies occupy spatially distinct structural epitopes on the surface of ricin. However, that assumption is being reconsidered because screening of a single domain camelid antibody (V_HH) library derived from two immunized alpacas revealed an apparent overlap between PB10 and toxin-neutralizing, non-neutralizing and weakly neutralizing V_HHs [24]. We subsequently solved the X-ray crystal structures of five such V_HHs in complex with RTA [25]. One V_HH (E5) had potent TNA, two (D10, G11) had moderate TNA, one (G12) had weak TNA and one (A7) had no detectable TNA. Surprisingly, all five V_HHs recognized overlapping structural epitopes on RTA, although they differed in their buried surface areas and the degree to which made contact with three prominent secondary elements within RTA:

β-strand h (residues 113-117), α-helix D (residues 150-156), and α-helix B (residues 98-106).

The result of that study prompted us to investigate additional RTA-V_HH interactions focused around the epitope on RTA defined by PB10. Of particular interest is V_HH F5, which was identified as being as potent as E5 in terms of TNA [24]. That antibody has been characterized extensively *in vitro* and *in vivo* although the X-ray crystal structure has not been solved [24,26,27]. We now report the X-ray crystal structure of F5 in complex with RTA, which we compare in detail to E5. We also rescreened our original V_HH library and identified another weakly neutralizing antibody called F8. We report the X-ray crystal structure of F8 in complex with RTA and demonstrate that F8's structural epitope is essentially nested within F5's neutralizing epitopes on the surface of RTA.

Materials and Methods

Toxin, secondary antibodies and other reagents

Ricin toxin (RCA-II) and RTA were obtained from Vector Laboratories (Burlingame, CA). HRP-anti-E-tag mAb and HRP-anti-M13 Ab were purchased from GE Healthcare (Piscataway Township, NJ). All other chemicals and reagents were purchased from Sigma-Aldrich (St. Louis, MO) unless noted otherwise.

ELISA and SPR

ELISA were done as previously described [24]. Nunc-Immuno plates (ThermoScientific, Swedesboro, NJ) were coated overnight at 4°C with 1 μg/mL target antigen (e.g., ricin), blocked for 2 h with 2% goat serum in 0.1% PBST and then incubated for 1 h with five-fold serial dilutions of V_HHs. For competition assays, murine IgGs (1 ug/mL) were coated onto wells overnight, then blocked for 2 hours. In a separate dilution plate, VHHs were diluted into biotinylated-ricin at the fixed EC_{90} concentration for each individual coated mAb. These mixtures were then transferred into the mAb coated plates and allowed to bind for 1 hour. After washing, bound biotinylated-ricin was detected with Streptavidin-HRP (1:1000) (ThermoFisher), and developed with SureBlue Peroxidase Substrate (KPL). The reaction was quenched with 1M phosphoric acid and absorbance was read at 450 nm using a VersaMax Microplate Reader (Molecular Devices, Sunnyvale, CA). F8's affinity for ricin was determined by surface plasmon resonance (SPR) using the ProteOn XPR36 (Bio-Rad Inc. CA, USA), as described previously [25].

Screening alpaca library for RTA-specific V_HHs

Antibody JIV-F5 (here referred to as simply F5 was described previously [24]. The RTA-specific V_HH JNM-F8 (here referred to as F8) was identified using the panning strategy described previously [24]. The original alpaca library was subjected to a low stringency (10 μg/ml target antigen) followed by a high stringency (1 μg/ml target antigen) panning on RTA coated onto Nunc Immunotubes. Following the second round of panning, 95 individual *E. coli* colonies were picked and grown overnight at 37° in a 96-well plate. A replica plate was then prepared, cultured, induced with IPTG and the supernatant assayed for RTA binding by ELISA.

Vero cell cytotoxicity assays

The Vero cell cytotoxicity assay ha been described in detail elsewhere [28]. Vero cells grown in DMEM containing 10% FBS were seeded (5×10^4 per mL) in 96 well cell culture plates and incubated at 37°C overnight. The cells were then overlaid with ricin (10 ng/mL, 150 pM) in the absence or presence of 5-fold serial dilutions of VHHs, and incubated at 37°C for 2 h. The cells were then washed and fresh medium applied. Cell viability was assessed 45-48 h later using CellTiter-Glo (Promega, Madison, WI).

Cloning, expression, and purification of V_HH F5 and F8

PCR amplicons corresponding to F5 (residues 1-127) and F8 (residues 1-137) VHHs were subcloned into the N-terminally deca-histidine maltose binding protein tagged MCSG9 expression vector using a standard ligase independent cloning protocol. Both V_HH proteins were expressed in *E. coli* strain BL21(DE3)-pRARE. The transformed bacteria were grown at 37°C in TB medium and induced at 20°C with 0.1 mM IPTG at an OD600 of 0.6 for ~16 hours. After induction, cells were harvested and resuspended in 20 mM Tris-Cl pH 7.5 and 150 mM NaCl. The cell suspension was sonicated and centrifuged at 30,000 × *g* for 30 minutes. After centrifugation, the V_HH-containing supernatant was purified by nickel-affinity and size-exclusion chromatography on an AKTAxpress system (GE Healthcare), which consisted of a 1 mL nickel affinity column followed by a Superdex 200 16/60 gel filtration column. The elution buffer consisted of 0.5M imidazole in binding buffer, and the gel filtration buffer consisted of 20 mM HEPES pH 7.6, 150mM NaCl, and 20mM imidazole. Fractions containing V_HH were pooled and subject to TEV protease cleavage (1:20 weight ratio) for 3 hours at room temperature in order to remove the decahistidine-maltose binding protein tag. The cleaved protein was passed over a 1mL Ni-NTA agarose (Qiagen) and 1 mL Amylose-agarose gravity column to remove the added TEV protease, cleaved residues, and uncleaved fusion protein. The plasmid pUTA-RTA encoding full length RTA was provided by Dr. Jon Robertus (UT Austin). RTA was expressed and purified as described previously [29,30]. In order to generate RTA-VHH protein complexes, after purification RTA was mixed in a 1:1 stoichiometry with the purified VHH and incubated on ice for 1 hour. Purified RTA-V_HH complex was concentrated to a final total concentration of 10 mg/ml for crystallization experiments.

Crystallization and data collection

Both RTA-V_HH complex crystals were grown by sitting drop vapor diffusion at 20°C using a protein to reservoir volume ratio of 1:1 with total drop volumes of 0.4 μL. Crystals of the RTA-F5 complex were grown against crystallization buffer containing 100 mM Tris-Cl (pH 4.5), 15% PEG 3000, 2.2 mM zinc zcetate, and 100 mM of dimethylbenzylammonium propane sulfonate. Crystals of the RTA-F5 complex nucleated within 24 hours and grew slowly to full size of ~60 μm over a period of 10 days. Crystals of the RTA-F8 complex were grown against crystallization buffer containing 100 mM BisTris pH 5.5, 25% PEG 3000, 260 mM NaCl, and 10 mM Tris (2carboxyethyl)phosphine hydrochloride. Crystals of the RTA-F8 complex nucleated within 24 hours and grew to full size of ~100 μm within 5 days. All crystals were flash frozen in liquid nitrogen after a short soak in the appropriate crystallization buffers supplemented with 20-25% ethylene glycol. Data were collected at

the 24-ID-C and 24-ID-E beamlines at the Advanced Photon Source, Argonne National Labs. The RTA-F5 data was indexed, merged, scaled, and converted to structure factors using XDS [31]. The RTA-F8 data was indexed, merged, and scaled using HKL2000 [32] then converted to structure factors using CCP4 [33].

Structure Determination and Refinement

The structures of both RTA- V_HH complexes were solved by molecular replacement using the program Phaser [34]. Molecular replacement calculations were performed using the coordinates of the ricin a chain as a search model for RTA (PDB: 1RTC) in both RTA- V_HH complexes. The V_HH coordinates used as a search model for both RTA- V_HH complexes was D10 (PDB: 4LGR) with all three of the CDRs removed from the search model. The resulting phase information was used to autobuild most of the model for the both RTA-VHH structures using the program ARP [35]. Some additional manual building of each model was performed with COOT [36]. All structural refinement was done employing the PHENIX package [37]. Twinned refinement was performed for the RTA-F8 complex using the twin operator -k,-h,-l with a twinning fraction of 0.04. During refinement a cross-validation test set was created from a random 5% of the reflections. Data collection and refinement statistics are listed in Table S1. Molecular graphics were prepared using PyMOL (Schrodinger) (DeLano Scientific LLC, Palo Alto, CA).

Accession Numbers

The structures generated in this study were deposited in the Protein Data Bank (PDB; http://www.rcsb.org/pdb/) under accession numbers 4Z9K (F5) and 5E1H (F8), as described in Table 1.

Results and Discussion

To identify additional Cluster I-specific VHHs, a previously described ricin-specific alpaca V_HH phage display library was subjected to panning on RTA-coated immunotubes, as described in the Materials and Methods. We identified seven new RTA-specific V_HHs, although none had IC_{50} values as potent as E5 or F5 (e.g., 5 nM) (D. Vance, C. Shoemaker, J. Tremblay, and N. Mantis, manuscript in preparation). For this specific study, we chose to pursue V_HH F8 because of its competitive inhibition profile with PB10 but not cluster II-IV murine mAbs SyH7, IB2 and GD12 (Figure 1). By ELISA, F8's EC_{50} for ricin holotoxin was 0.5-0.8 nM and its dissociation constant (K_D) determined by SPR was 0.2 nM (Table 2; Figure 2). In the Vero cell cytotoxicity assay, F8 had an IC_{50} of ∼300 nM, thereby classifying it as a weak neutralizing antibody. This is in contrast to F5, which has an IC_{50} of ∼5 nM (Figure 2).

X-ray crystallography of V_HH-RTA complexes

To elucidate the exact epitopes recognized by F5 and F8, we solved the X-ray crystal structures of each of the two V_HHs in complex with RTA. The crystal structures of RTA-F5 and RTA-F8 were solved at 1.5 Å and 2.0 Å, respectively (Table 1; Table S1; Figure 3). In both cases, the V_HHs assumed a classical immunoglobulin fold consisting of nine β-strands arranged in two β-sheets with CDRs 1-3 on one face of the molecule. There were two 3_{10}

helices in the case of F5 and five 3_{10} helices in the case of F8 (Figure 4). Superimposing the Cα atoms of RTA from the RTA-F5 and RTA-F8 crystal structures onto recombinant RTA (PDB: **1RTC)** revealed an RMSD of 0.6 Å for each, indicating that neither F5 nor F8 induce RTA to undergo any significant conformational changes.

F5 had two intramolecular disulfide bridges: the canonical V_HH disulfide bond that links FR1 to FR3 via Cys22 and Cys92, and the less frequently observed secondary disulfide bond that links CDR2 and CDR3 via Cys50 and Cys97 (Figure S1A). It is interesting to note that these two disulfide bonds are also present in E5, which we will discuss in more detail below. F8, on the other hand, was somewhat unusual in that it did not form the canonical disulfide bond between FR1 residue Cys22 and FR3 residue Cys96 (Figure S1B). We postulate that this is a crystallization artifact as crystal contacts formed between residues immediately C-terminal to Cys22 slightly perturb its position relative to Cys96 resulting in a gap of 6.8 Å that precludes formation of the disulfide bond.

Interactions of F5 with RTA

F5 made contact with RTA's α–helix B (residues 98, 101, 102, 104, and 105) along with several residues immediately before α–helix B (residues 91, 92, 94, 95, 96, 97). F5 also interacted with β–strand h (residues 113-117) as well as a few residues in the loops just before and after β–strand h (residues 111,112 and 118,119), and the C-terminal region of α–helix D (residue 154) along with the loop immediately following this helix (residues 157, 161). F5 also contacted Arg125 within α-helix C (Figure 5A).

Overall, F5 and E5 interact with RTA in a very similar manner (PDB: **4LGP**) (Figure 3). As highlighted in Table 2, F5 and E5 buried similar amounts of solvent-exposed surface area on RTA (1755-1760 $Å^2$). Although F5 formed fewer hydrogen bonds with RTA (9 H-bonds) than E5 (16 H-bonds), the two antibodies are similar in that all three CDRs contribute to the hydrogen-bonding network with RTA. For example, F5's CDR1 buried 550 $Å^2$ on RTA and generated 4 H-bonds, including two (Asp31, Tyr32) focused on Tyr154 in RTA's α–helix D. E5's CDR1 also H-bonds with Tyr154 by virtue of residues His31 and Tyr32. At this point in time it is not known whether Tyr154 is significant in terms of toxin-neutralizing activity or whether it simply affords a conveniently located solvent exposed side chain available for H-bond formation.

F5's CDR2 buried 293 $Å^2$ and formed a single hydrogen bond between Asp53 and Ala118 located just beyond the C-terminus of RTA's β–strand h. E5's CDR2 accomplished the same task except that contact with Ala118 was mediated by Arg52. There was also one salt-bridge formed between Asp53 within the CDR2 of F5 and Arg125 in RTA. F5's CDR3 buried 856 $Å^2$ and formed 4 H-bonds with RTA's β–strand h (residues 112,114,116, 118), which is the same number of H-bonds formed between E5 and β–strand h region (residues 113,115,116,118). F5 and E5's CDR3 regions also interacted to a similar extent with α-helix B, albeit by different molecular interactions. F5's interface was mediated by van der Waals interactions, while E5's CDR3 also formed van der Waals interactions and a single H-bond between Arg104 and RTA's Thr105 (Table 2; Figure 5A,B).

It should be noted that F5's CDR3, like E5's CDR3, is spatially constrained by a disulfide bond between Cys50 and Cys97 (Cys50 and Cys100 in E5). The CDR3s of F5 and E5 are further restrained by two hydrophobic interactions between certain CDR3 and FR residues. In F5 those interactions occur between CDR3 residue Val101and FR residues Phe37 and Tyr57, and CDR3 residue Leu103 with FR residues Phe37 and Trp109 (Figure 6A). Analogous CRD3-FR residue interactions are observed in E5 (e.g., CDR3 residue Tyr101 with FR residues Trp47 and Val59, and CDR3 residue Trp103 with FR residues Val97 and Trp107) (Figure 6B). The longer CDR3 within F5 formed an additional hydrophobic interaction between CDR3 residue Leu99 and FR residue Tyr57 that is not present in E5 (Figure 6). Altogether, the disulfide bonds and hydrophobic interactions were evenly distributed throughout the CDR3 of F5 and E5 with the disulfide bond occurring near the beginning of the CDR3 segment and the hydrophobic interactions forming in the middle and terminal regions of each CDR3 sequence. The uniformed tethering of the CDR3 region to the VHH surface caused by these interactions made both CDR3s similarly compact, with a comparable conformation, despite their differences in sequence length (16 residues in F5, 10 residues in E5) and low sequence identity of 19% (Figure 6C).

As mentioned above, F5 and E5 bind equivalently to α-helix B (bsa = 477 $Å^2$ and 472 $Å^2$, respectively), a trait that we propose is associated with potent neutralizing activity. Exactly how F5 and E5 interact with α-helix B is different, however, and is worth discussing in more detail. The first consideration is that F5's CDR3 is six residues longer than E5's. As a result F5's CDR3 runs along the axis of α-helix B towards its N-terminus (residues 98, 101), resulting in the burial an additional 50 $Å^2$ relative to E5 (Figure 7A). This gain in buried surface area is offset by Phe106 in F5's CDR3, which intercalates between RTA's α-helix B and β–strand h and positions F5's CDR3 away from the C-terminal portion of α-helix B at residues 105, 106. In contrast, E5's Arg104 forms an H-bond with RTA's Thr105, the penultimate residue in α-helix B (Figure 7A). As a consequence E5 buries an additional 57 Å2 of buried surface area (at RTA residues 105, 106), as compared to F5.

Other factors contribute to the structural differences between F5 and E5, which have an RMSD of 1.8 Å for all Cα atoms. For example, the last seven C-terminal residues within F5's CDR3 (residues 103-109) assume a different configuration relative E5 (residues 102-107). F5's CDR3 residue Leu103 forms a hydrophobic interaction with FR residue Trp109. The intervening residues, Ile104, Asp105, and Phe106, “pucker” to permit the Leu103-Trp109 hydrophobic interaction to occur. Incidentally, the puckering occurs in the direction of RTA, forcing RTA to rotate away from the protruding CDR3 residues and ultimately resulting in a rigid body rotation of RTA of ∼17.3° centered around the axis of β-strand H relative to RTA within the RTA-E5 complex (Figure 7B). While there is an analogous hydrophobic interaction between CDR3 residue Trp103 and FR residue Trp107 of E5, the puckering effect does not occur because the intervening spacer between residues 103-107 is three residues not five.

Interactions of F8 with RTA

The RTA-F8 crystal structure revealed that it buried a total surface area of 1103 $Å^2$ on RTA. F8's principal contacts with RTA were centered on β–strand h, with lesser interactions

occurring with α–helix B and α–helix D. The CDR3 buried 838 Å^2 on RTA and accounted for 8 of the 9 intermolecular hydrogen bonds with β–strand h (Table 2; Figure 8A). The most notable interaction involves five main chain hydrogen bonds between the CDR3 β–strand (residues 103-107) and RTA's β–strand h (residues 113-117). In this configuration, the CDR3-derived β–strand becomes, in essence, the seventh β–strand within RTA's centrally located β–sheet. The ninth H-bond occurred between Tyr102 and RTA residue Tyr154. This interaction is interesting because, as noted above, both E5 and F5 form H-bonds with Tyr154, albeit through residues located in CDR1 not CDR3. Other notable associations that occur between F8 and RTA include Lys31 (CDR1) and Trp53 (CDR2) with RTA residues His94 and Pro95, resulting in a total buried surface area of 190 Å^2.

The structure of the RTA-F8 complex is strikingly similar to the previously solved structure of RTA bound to V_HH G12 (PDB: **4LGS**). The total surface areas buried by F8 and G12 were nearly identical (1103 Å^2 versus 1100 Å^2, respectively). The RMSD between F8 and G12 was 1.1Å for all Cα atoms, which was not expected considering that the two antibodies share limited overall sequence identity (72.0%) and very little identity (36.4%) within CDR3 (Figure 8B; Figure S2A). The basis of the similarity between F8 and G12 can be explained by a number of factors. First, CDR3s from both antibodies extended outward in identical conformations from their respective V_HH surfaces (Figure 8B). As a consequence, F8 and G12's CRD3s form essentially the same β–sheet interaction with RTA's β–strand h. F8 and G12 also display a similar pattern of hydrophobic interactions between FR and CDR3 residues, which renders the N-terminal elements of CDRs unrestrained (Figure 8C,D; Figure S2A). Since the CDR3s of F8 and G12 are identical in length (22 residues), the two V_HH s have the same number of unrestrained N-terminal residues that interact with RTA's β–strand h in a similar fashion (Figure 9A). When those key hydrophobic interactions between the CDR3 and FR residues are not present, as in the case of VHH G11 (PDB: **4LHJ**), the entire CDR3 extends much further away from the V_HH, resulting in fundamentally different interaction with RTA (Figure 9B). Indeed, sequence analysis of additional structural homologs of F8 revealed that, as a rule, V_HHs with a large hydrophobic residue within the CDR3 positioned three residues from the end of their CDR3, combined with similarly positioned hydrophobic residues within the central region of the CDR3 and FR areas results in an overall constrained CDR3 (Figure S3).

Conclusions and significance

We have now solved the X-ray crystal structures of seven different Cluster I V_HHs in complex with RTA [25]. At the structural level, Cluster I encompasses α–helix B (residues 98-106), β–strand h (residues 113-117), and the C-terminus of α–helix D (residues 154-156). In terms of toxin-neutralizing activities, two V_HHs had potent TNA (E5, F5), one had moderate TNA (D10), three had weak TNA (G11, G12, F8) and one was devoid of any detectable TNA (A7). Within these seven antibodies, toxin-neutralizing activity positively correlated with total buried surface area (Table 2) with the epitopes recognized by weak and non-neutralizing antibodies nested within epitopes recognized by highly potent toxin-neutralizing antibodies. For example, E5 and F5 each bury ∼1760 Å^2 of solvent-exposed surface area on RTA, whereas F8, G11, G12, A7 each bury only ∼1100 Å^2. The extent to which the VHHs interacted with α–helix B (residues 98-106) and α–helix D (residues

154-156) accounted for the overall differences in buried surface area and, therefore, also correlated with enhanced toxin-neutralizing capacity. The strongest neutralizers E5 and F5 make substantial contacts with α–helix B, while the moderate neutralizing antibody D10 interacts primarily with α–helix D. Overall, α-helix B, and specifically Thr105, appear to constitute a “neutralizing hot spot” within RTA's epitope Cluster I. The weak and non-neutralizing antibodies F8, G12, G11 and A7 interact almost exclusively with β–strand h and have relatively long CDR3s (15-22 residues) that protruded away from the surface of the VHH.

The observation that non-neutralizing structural epitopes are essentially nested within toxin-neutralizing epitopes on the surface of RTA has implications for developing a surrogate assay to measure the efficacy of ricin toxin subunit vaccines in humans. Standard cell-based toxin-neutralizing assays are time consuming and susceptible to variability [28]. In an effort to identify additional surrogate measures of protection, we developed a direct competition ELISA using three different Cluster I toxin-neutralizing mAbs (i.e., PB10, R70 and WECB2) against sera from Rhesus macaques that had been immunized with RiVax and challenged with ricin by the aerosol route [38]. We also performed competition ELISAs with sera from RiVax vaccinated humans. We reasoned that the degree to which an individual serum sample inhibited a toxin-neutralizing mAb from binding to ricin might serve as a surrogate measure of toxin-neutralizing activity in that serum sample. However, interpretation of these ELISAs is confounded if neutralizing and non-neutralizing antibodies recognize overlapping epitopes and can compete with each other for real estate on the surface of RTA. While we do not have any direct evidence of neutralizing and non-neutralizing antibodies interfering with each other *in vivo*, we have demonstrated this phenomenon *in vitro* (Y. Rong, G. Van Slyke and N. Mantis, manuscript in preparation).

A more detailed understanding of what constitutes neutralizing and non-neutralizing structural B cell epitopes on RTA may prove useful in subunit vaccine development. For example, identifying strategies to better “present” α-helix B, and specifically residue Thr105, through antigen “resurfacing” could focus antibody responses against this region of RTA and possibly boost the overall proportion of toxin-neutralizing antibodies within a polyclonal population. Resurfacing strategies (including scaffolding approaches) have proven powerful in refining HIV subunit vaccine antigens like gp120 and gp41 [39,40]. We have already applied computational modeling as a means to improve the immunogenicity of RiVax [41,42]. It is interesting that factors that influenced the rigidity of α-helix B in the context of RiVax correlated with enhanced onset of toxin-neutralizing antibodies when the RiVax point mutants were tested as vaccines in mice. With the elucidation of the E5 and F5 structural epitopes will are now in a position to revisit computational modeling with a specific focus on key resides that are thought to be critical in eliciting potent neutralizing antibodies.

Supplementary Material

Refer to Web version on PubMed Central for supplementary material.

Acknowledgments

We gratefully acknowledge the 24-ID-C and 24-ID-E beamline staff at the Advanced Photon Source for their assistance in data collection and Dr. Jon Robertus (University of Texas, Austin) for providing us with a plasmid encoding RTA. We also thank Ms. Jacque M. Tremblay (Tufts University) for her contributions to the VHH identification. This work was supported by Contract No. HHSN272201400021C from the National Institutes of Allergy and Infectious Diseases. Use of the National Synchrotron Light Source, Brookhaven National Laboratory, was supported by the U.S. Department of Energy, Office of Science, Office of Basic Energy Sciences, under contract no. DE-AC02-98CH10886. The authors declare no conflicts of interest related to this study.

References Cited

1. Mantis, NJ. Ricin Toxin. In: Liu, D., editor. Manual of Security Sensitive Microbes and Toxins. CRC Press; 2014. p. 1024
2. Schrot J, Weng A, Melzig MF. Ribosome-inactivating and related proteins. Toxins (Basel). 2015; 7(5):1556–1615. [PubMed: 26008228]
3. Katzin BJ, Collins EJ, Robertus JD. Structure of ricin A-chain at 2.5 A. Proteins. 1991; 10(3):251–259. [PubMed: 1881881]
4. Endo Y, Mitsui K, Motizuki M, Tsurugi K. The mechanism of action of ricin and related toxins on eukaryotic ribosomes. J Biol Chem. 1987; 262:5908–5912. [PubMed: 3571242]
5. Endo Y, Tsurugi K. RNA N-glycosidase activity of ricin A-chain. Mechanism of action of the toxic lectin ricin on eukaryotic ribosomes. J Biol Chem. 1987; 262(17):8128–8130. [PubMed: 3036799]
6. Rutenber E, Ready M, Robertus JD. Structure and evolution of ricin B chain. Nature. 1987; 326(6113):624–626. [PubMed: 3561502]
7. Spooner RA, Lord JM. How Ricin and Shiga Toxin Reach the Cytosol of Target Cells: Retrotranslocation from the Endoplasmic Reticulum. Curr Top Microbiol Immunol. 2012; 357:19–40. [PubMed: 21761287]
8. McHugh CA, Tammariello RF, Millard CB, Carra JH. Improved stability of a protein vaccine through elimination of a partially unfolded state. Protein Sci. 2004; 13(10):2736–2743. [PubMed: 15340172]
9. Smallshaw JE, Firan A, Fulmer JR, Ruback SL, Ghetie V, Vitetta ES. A novel recombinant vaccine which protects mice against ricin intoxication. Vaccine. 2002; 20(27-28):3422–3427. [PubMed: 12213413]
10. Vance DJ, Mantis NJ. Progress and Challenges Associated with the Development of Ricin Toxin Subunit Vaccines. Expert review of vaccines. 2016
11. Montfort W, Villafranca JE, Monzingo AF, Ernst SR, Katzin B, Rutenber E, Xuong NH, Hamlin R, Robertus JD. The three-dimensional structure of ricin at 2.8 A. Journal of Biological Chemistry. 1987; 262(11):5398–5403. [PubMed: 3558397]
12. Rutenber E, Katzin BJ, Ernst S, Collins EJ, Mlsna D, Ready MP, Robertus JD. Crystallographic refinement of ricin to 2.5 A. Proteins. 1991; 10(3):240–250. [PubMed: 1881880]
13. Dai J, Zhao L, Yang H, Guo H, Fan K, Wang H, Qian W, Zhang D, Li B, Wang H, Guo Y. Identification of a novel functional domain of ricin responsible for its potent toxicity. J Biol Chem. 2011; 286(14):12166–12171. [PubMed: 21303906]
14. Lebeda FJ, Olson MA. Prediction of a conserved, neutralizing epitope in ribosome-inactivating proteins. Int J Biol Macromol. 1999; 24(1):19–26. [PubMed: 10077268]
15. Lemley PV, Amanatides P, Wright DC. Identification and characterization of a monoclonal antibody that neutralizes ricin toxicity in vitro and in vivo. Hybridoma. 1994; 13(5):417–421. [PubMed: 7860097]
16. O'Hara JM, Neal LM, McCarthy EA, Kasten-Jolly JA, Brey RN 3rd, Mantis NJ. Folding domains within the ricin toxin A subunit as targets of protective antibodies. Vaccine. 2010; 28:7035–7046. [PubMed: 20727394]
17. Smallshaw JE, Ghetie V, Rizo J, Fulmer JR, Trahan LL, Ghetie MA, Vitetta ES. Genetic engineering of an immunotoxin to eliminate pulmonary vascular leak in mice. Nat Biotechnol. 2003; 21(4):387–391. [PubMed: 12627168]

18. Carra JH, Wannemacher RW, Tammariello RF, Lindsey CY, Dinterman RE, Schokman RD, Smith LA. Improved formulation of a recombinant ricin A-chain vaccine increases its stability and effective antigenicity. Vaccine. 2007; 25(21):4149–4158. [PubMed: 17408819]
19. Olson MA, Carra JH, Roxas-Duncan V, Wannemacher RW, Smith LA, Millard CB. Finding a new vaccine in the ricin protein fold. Protein engineering, design & selection: PEDS. 2004; 17(4):391–397. [PubMed: 15187223]
20. O'Hara JM, Yermakova A, Mantis NJ. Immunity to ricin: fundamental insights into toxin-antibody interactions. Curr Top Microbiol Immunol. 2012; 357:209–241. [PubMed: 22113742]
21. Yermakova A, Mantis NJ. Protective immunity to ricin toxin conferred by antibodies against the toxin's binding subunit (RTB). Vaccine. 2011; 29(45):7925–7935. [PubMed: 21872634]
22. O'Hara JM, Kasten-Jolly JC, Reynolds CE, Mantis NJ. Localization of non-linear neutralizing B cell epitopes on ricin toxin's enzymatic subunit (RTA). Immunol Lett. 2014; 158(1-2):7–13. [PubMed: 24269767]
23. Vance DJ, Mantis NJ. Resolution of two overlapping neutralizing B cell epitopes within a solvent exposed, immunodominant alpha-helix in ricin toxin's enzymatic subunit. Toxicon. 2012; 60(5): 874–877. [PubMed: 22750533]
24. Vance DJ, Tremblay JM, Mantis NJ, Shoemaker CB. Stepwise engineering of heterodimeric single domain camelid VHH antibodies that passively protect mice from ricin toxin. J Biol Chem. 2013; 288(51):36538–36547. [PubMed: 24202178]
25. Rudolph MJ, Vance DJ, Cheung J, Franklin MC, Burshteyn F, Cassidy MS, Gary EN, Herrera C, Shoemaker CB, Mantis NJ. Crystal structures of ricin toxin's enzymatic subunit (RTA) in complex with neutralizing and non-neutralizing single-chain antibodies. J Mol Biol. 2014; 426(17):3057–3068. [PubMed: 24907552]
26. Herrera C, Tremblay JM, Shoemaker CB, Mantis NJ. Mechanisms of Ricin Toxin Neutralization Revealed through Engineered Homodimeric and Heterodimeric Camelid Antibodies. J Biol Chem. 2015; 290(46):27880–27889. [PubMed: 26396190]
27. Herrera C, Vance DJ, Eisele LE, Shoemaker CB, Mantis NJ. Differential Neutralizing Activities of a Single Domain Camelid Antibody (VHH) Specific for Ricin Toxin's Binding Subunit (RTB). PLoS One. 2014; 9(6):e99788. [PubMed: 24918772]
28. Wahome PG, Mantis NJ. High-throughput, cell-based screens to identify small-molecule inhibitors of ricin toxin and related category b ribosome inactivating proteins (RIPs). Curr Protoc Toxicol. 2013; Chapter 2:23. Unit 2. [PubMed: 23408195]
29. Lewis MS, Youle RJ. Ricin subunit association. Thermodynamics and the role of the disulfide bond in toxicity. J Biol Chem. 1986; 261(25):11571–11577. [PubMed: 3745156]
30. Villafranca JE, Robertus JD. Crystallographic study of the anti-tumor protein ricin. J Mol Biol. 1977; 116(2):331–335. [PubMed: 599561]
31. Kabsch W. Integration, scaling, space-group assignment and post-refinement. Acta Crystallogr D Biol Crystallogr. 2010; 66(Pt 2):133–144. [PubMed: 20124693]
32. Otwinowski Z, Minor W. Processing of x-ray diffraction data collected in oscillation mode. Methods in Enzymology. 1997; 276:307–326.
33. Winn MD, Ballard CC, Cowtan KD, Dodson EJ, Emsley P, Evans PR, Keegan RM, Krissinel EB, Leslie AG, McCoy A, McNicholas SJ, Murshudov GN, Pannu NS, Potterton EA, Powell HR, Read RJ, Vagin A, Wilson KS. Overview of the CCP4 suite and current developments. Acta Crystallogr D Biol Crystallogr. 2011; 67(Pt 4):235–242. [PubMed: 21460441]
34. McCoy AJ, Grosse-Kunstleve RW, Adams PD, Winn MD, Storoni LC, Read RJ. Phaser crystallographic software. J Appl Crystallogr. 2007; 40(Pt 4):658–674. [PubMed: 19461840]
35. Morris RJ, Perrakis A, Lamzin VS. ARP/wARP and automatic interpretation of protein electron density maps. Methods Enzymol. 2003; 374:229–244. [PubMed: 14696376]
36. Emsley P, Lohkamp B, Scott WG, Cowtan K. Features and development of Coot. Acta Crystallogr D Biol Crystallogr. 2010; 66(Pt 4):486–501. [PubMed: 20383002]
37. Adams PD, Afonine PV, Bunkoczi G, Chen VB, Davis IW, Echols N, Headd JJ, Hung LW, Kapral GJ, Grosse-Kunstleve RW, McCoy AJ, Moriarty NW, Oeffner R, Read RJ, Richardson DC, Richardson JS, Terwilliger TC, Zwart PH. PHENIX: a comprehensive Python-based system for

macromolecular structure solution. Acta Crystallogr D Biol Crystallogr. 2010; 66(Pt 2):213–221. [PubMed: 20124702]

38. Roy CJ, Brey RN, Mantis NJ, Mapes K, Pop IV, Pop LM, Ruback S, Killeen SZ, Doyle-Meyers L, Vinet-Oliphant HS, Didier PJ, Vitetta ES. Thermostable ricin vaccine protects rhesus macaques against aerosolized ricin: Epitope-specific neutralizing antibodies correlate with protection. Proc Natl Acad Sci U S A. 2015; 112(12):3782–3787. [PubMed: 25775591]
39. Correia BE, Ban YE, Friend DJ, Ellingson K, Xu H, Boni E, Bradley-Hewitt T, Bruhn-Johannsen JF, Stamatatos L, Strong RK, Schief WR. Computational protein design using flexible backbone remodeling and resurfacing: case studies in structure-based antigen design. J Mol Biol. 2011; 405(1):284–297. [PubMed: 20969873]
40. Wu X, Yang ZY, Li Y, Hogerkorp CM, Schief WR, Seaman MS, Zhou T, Schmidt SD, Wu L, Xu L, Longo NS, McKee K, O'Dell S, Louder MK, Wycuff DL, Feng Y, Nason M, Doria-Rose N, Connors M, Kwong PD, Roederer M, Wyatt RT, Nabel GJ, Mascola JR. Rational design of envelope identifies broadly neutralizing human monoclonal antibodies to HIV-1. Science. 2010; 329(5993):856–861. [PubMed: 20616233]
41. Thomas JC, O'Hara JM, Hu L, Gao FP, Joshi SB, Volkin DB, Brey RN, Fang J, Karanicolas J, Mantis NJ, Middaugh CR. Effect of single-point mutations on the stability and immunogenicity of a recombinant ricin A chain subunit vaccine antigen. Human vaccines & immunotherapeutics. 2013; 9(4):740–748.
42. Wahome N, Sully E, Singer C, Thomas JC, Hu L, Joshi SB, Volkin DB, Fang J, Karanicolas J, Jacobs DJ, Mantis NJ, Middaugh CR. Novel Ricin Subunit Antigens With Enhanced Capacity to Elicit Toxin-Neutralizing Antibody Responses in Mice. J Pharm Sci. 2016

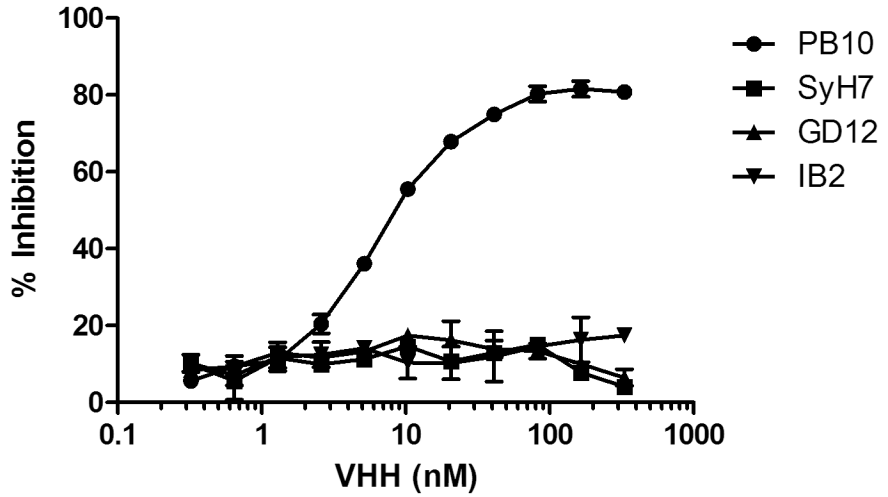

Figure 1. F8 recognizes a Cluster I epitope on RTA

VHH F8 was subject to competition ELISA with mAbs against epitope clusters I (PB10), II (SyH7), III (IB2), and IV (GD12), as described in Materials and Methods. The y-axis indicates the degree (%) of specific mAb binding inhibition in the presence of F8.

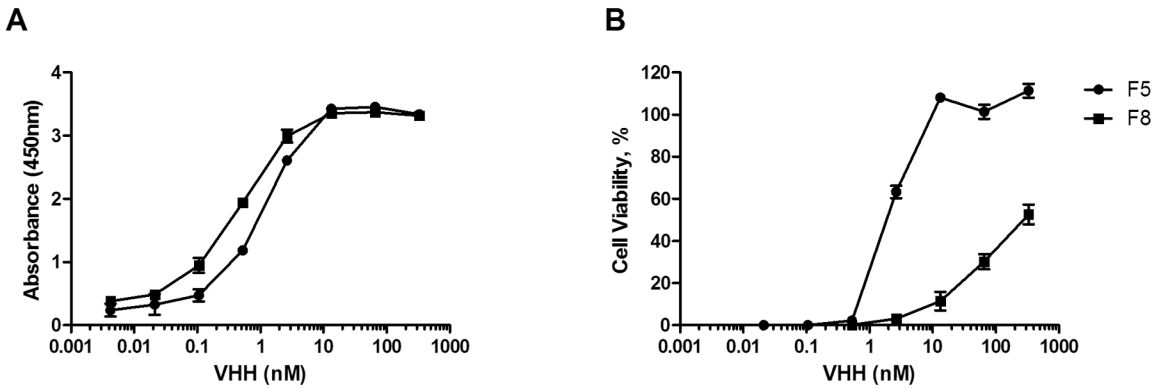

Figure 2. Binding and toxin-neutralizing activities associated with F5 and F8

(A) Relative affinities of F5 and F8 for ricin, as determined by direct ELISA in which ricin was captured in its native form on the microtiter plate wells via a surrogate receptor asialofetuin (ASF). EC_{50} values are defined as the antibody concentration that achieved half-maximal binding. (B) F5 and F8 were mixed at the indicated concentrations with ricin (10 ng/ml) in solution and then applied to Vero cells for cytotoxicity assessment, as described in Materials and Methods. IC_{50} values were based in the antibody concentration that conferred 50% viability. A single representative experiment done in triplicate is shown. The EC_{50} and IC_{50} determinations were done at least three independent times.

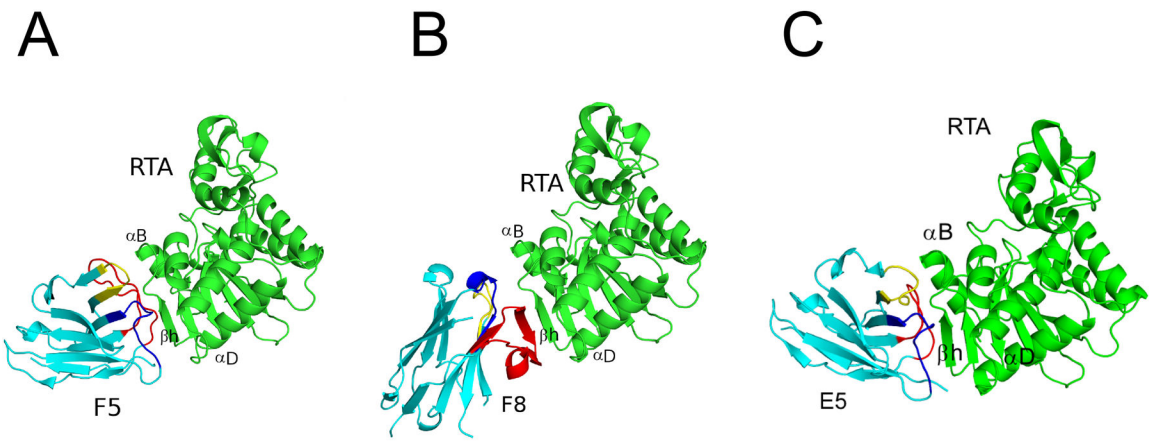

Figure 3. Structures of RTA-VHH complexes

X-ray crystal structures of RTA (green) in complex with neutralizing VHHs (A) F5, (B) F8 and (C) E5. The VHHs are colored cyan, with CDRs 1, 2, and 3 colored blue, yellow, and red, respectively. RTA secondary structural elements β–strand h (residues 113-117), α–helix B (residues 98-106), and α–helix D (residues 150-156) are indicated, as necessary. RTA is similarly oriented in each panel, highlighting the different VHH binding modes.

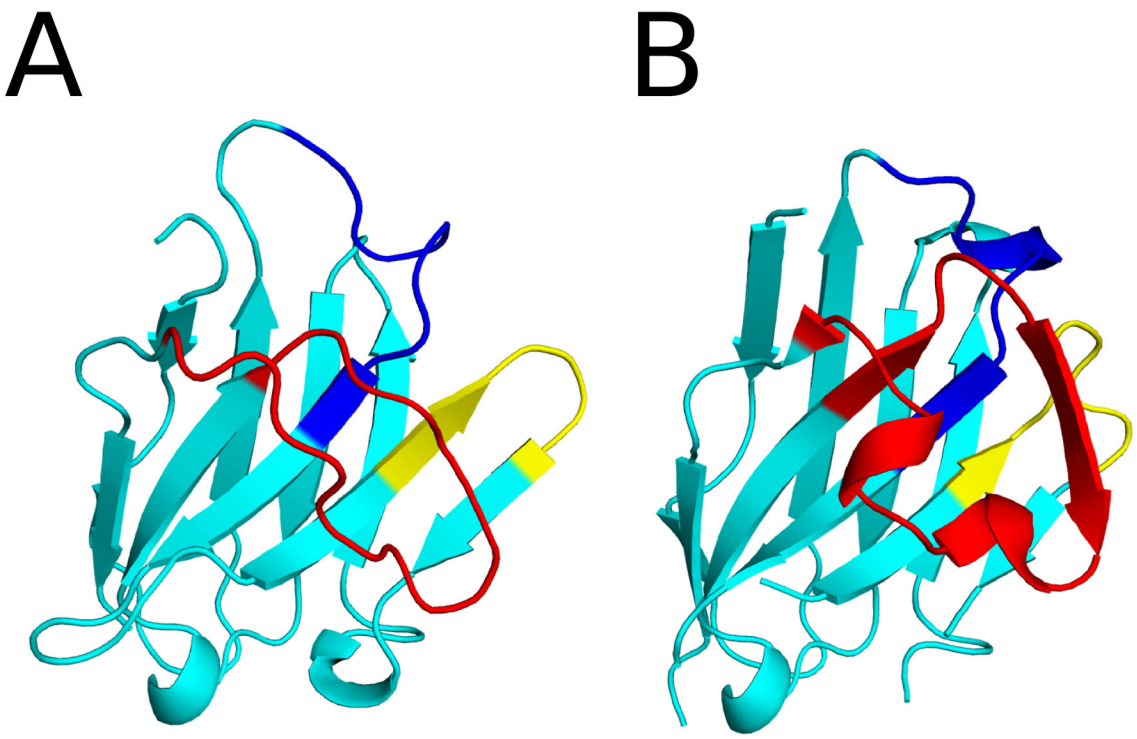

Figure 4. X-ray crystal structures of the F5 and F8 in complex with RTA

The structures of (A) VHH F5 and (B) VHH F8, drawn as ribbon diagrams with CDR 1, 2, and 3 colored blue, yellow, and red, respectively. Both VHHs are similarly oriented with CDR3 in front.

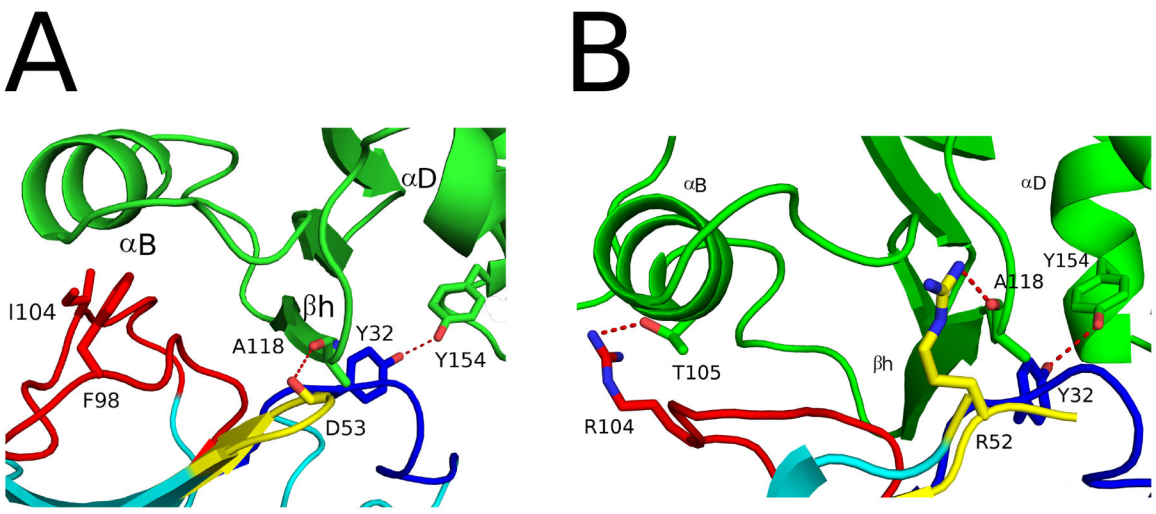

Figure 5. Comparison of F5 and E5 binding mode with key RTA secondary structural elements

RTA (green) and VHHs (cyan) are drawn as ribbon diagrams. VHH CDRs 1, 2, and 3 are colored blue, yellow, and red, respectively. Side chains are drawn as sticks and color coordinated to the main chain color. Hydrogen bonds are represented as red dashes. (A) Close-up of the interaction between VHH F5 and RTA's secondary structural elements α–helix B (residues 98-106), β–strand h (residues 113-117), and α–helix D (residue 154). Only two of the 9 hydrogen bonds are depicted for clarity. Two residues within the CDR3 (Phe94 and Ile114) that interact with α–helix B in RTA are also drawn as sticks and colored red. (B) Zoom in of the interface between VHH E5 and RTA depicting the analogous interactions between E5 and the same region of RTA. Only three hydrogen bonds are drawn for clarity.

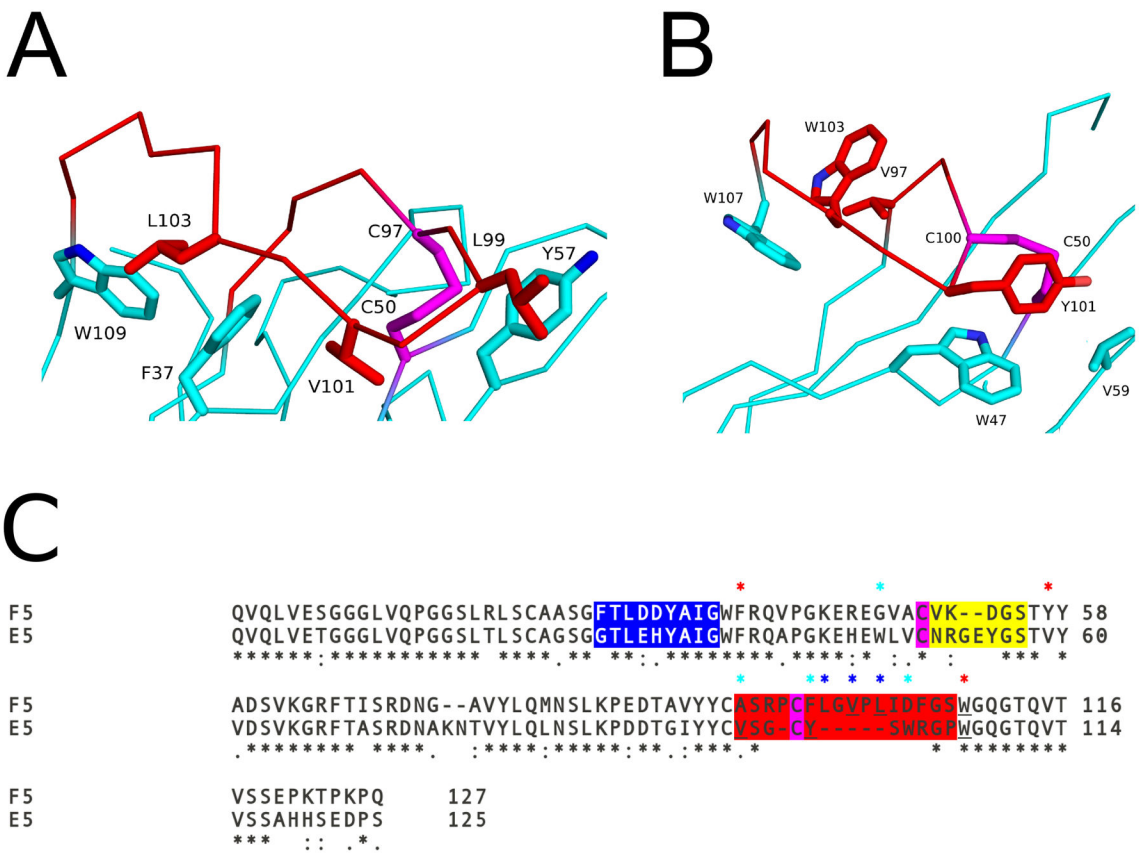

Figure 6. Key residues influencing CDR3 conformation

The Cα–traces of (A) VHH F5 and (B) VHH E5. The VHHs are colored cyan with their CDR3 elements colored red. Key residues forming hydrophobic interactions are drawn as sticks and color coordinated to their respective main chain color. The disulfide bond between residues Cys50-Cys97 in VHH F5, and Cys50-Cys100 in E5, are shown in stick representation and colored magenta. (C) Sequence alignment of F5 and E5. CDR1, 2, and 3 are highlighted with blue, yellow, and red, respectively. Cysteines forming the disulfide between the CDR3 and FR residues are in magenta. Sequence positions of residues involved in the hydrophobic interactions between the CDR3 and FR residues in both F5 and E5 are highlighted with red asterisks above the sequence. Residues participating in hydrophobic interactions for F5 alone are highlighted with a blue asterisk and E5 alone with cyan asterisk above the sequence. Black asterisks below the sequence denote sequence identity.

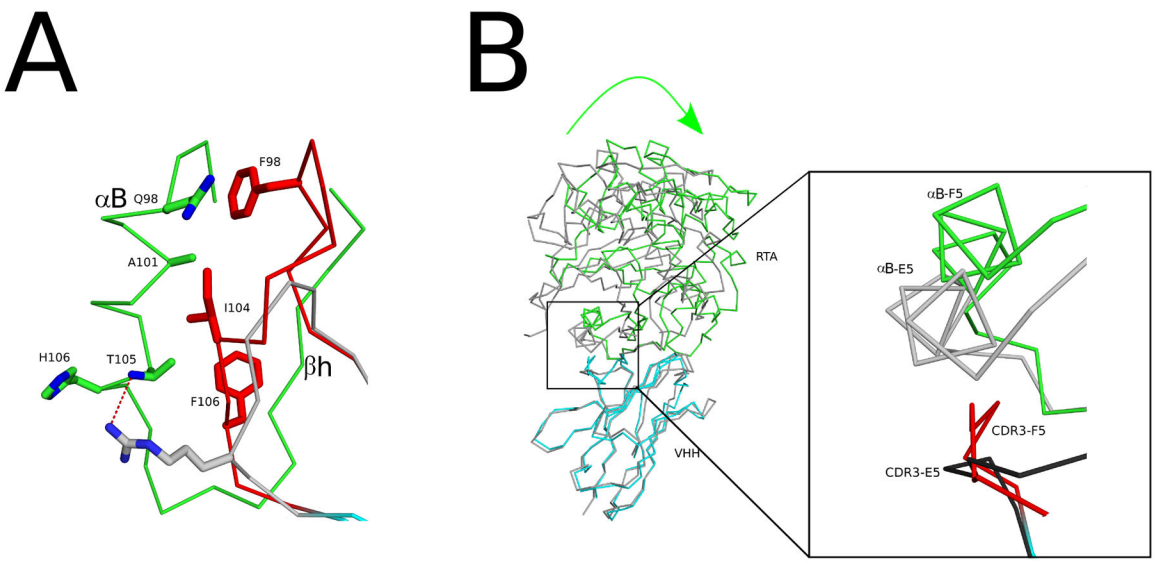

Figure 7. Different interactions with α-helix B in RTA

(A) Shown are the super positioned Cα–traces of the RTA-F5 complex with VHH E5. The CDR3 element in F5 is colored red, while CDR3 elements of VHHs E5 is colored gray. RTA is colored green. Key residues forming interactions are drawn as sticks and color coordinated to their respective main chain color. (B) The super positioned Cα-traces of RTA in complex with VHH F5 (green-cyan, respectively) and VHH E5 (gray-gray, respectively). The green arrow illustrates direction of the 17.3° rotation of F5 relative to E5 from the center of the RTA-VHH interface. The inset illustrates the more puckered conformation of the CDR3 from F5 colored red relative to the CDR3 region of E5 in dark gray. The more protracted conformation of the E5 CDR3 generates the relative rotation of the RTA subunit within the RTA-F5 complex compared to the RTA-E5 complex.

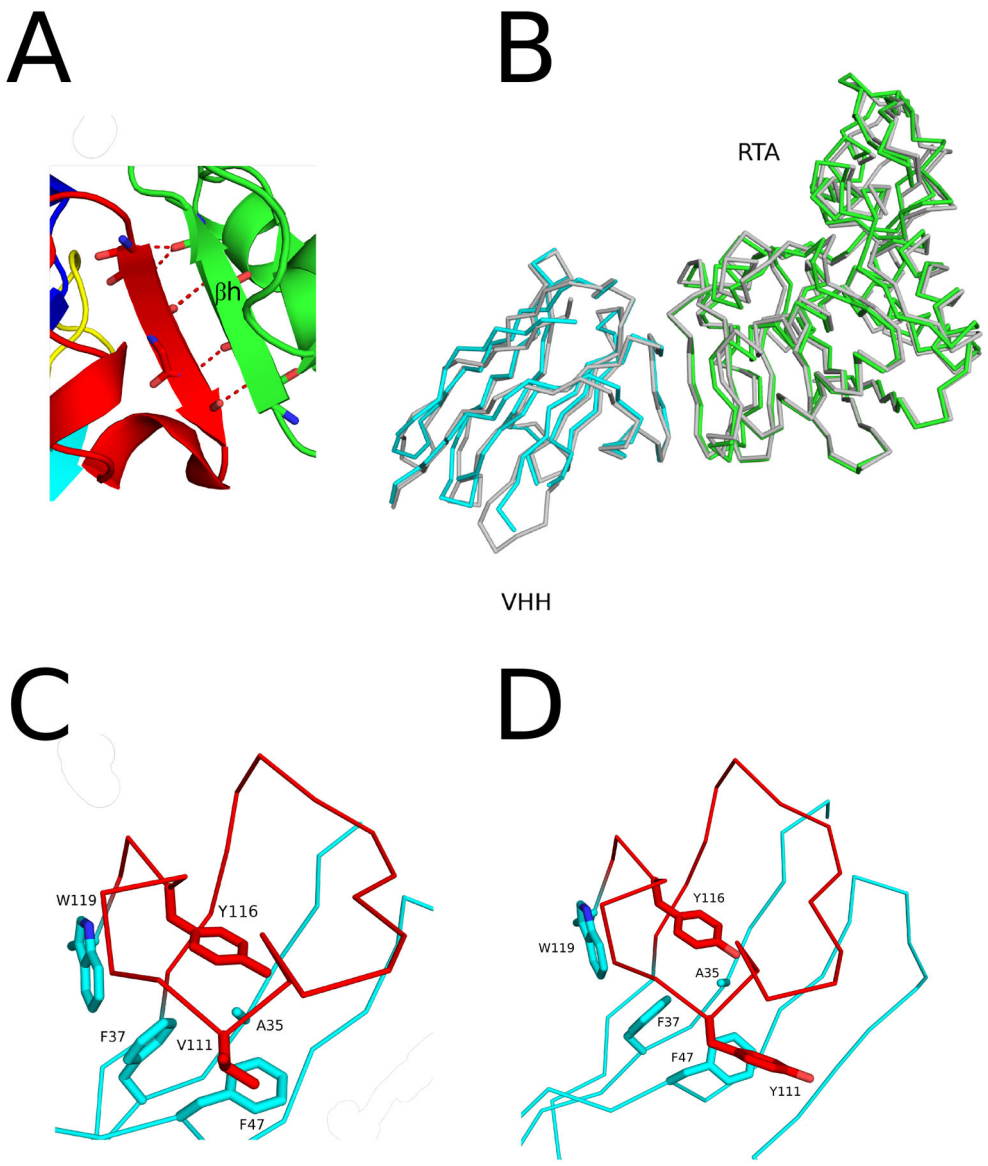

Figure 8. Close-up of of F5 CDR3 with RTA and key residues influencing F5 CDR3 conformation

(A) Zoom in of the interface between VHH F8 and RTA depicting the main-chain hydrogen bond interactions between the CDR3 from F8 with β–strand h (residues 113-117) in RTA. RTA (green) and VHHs (cyan) are drawn as ribbon diagrams. VHH CDRs 1, 2, and 3 are colored blue, yellow, and red, respectively. Main chain atoms are drawn as sticks and color coordinated to the main chain color. Hydrogen bonds are represented as red dashes. (B) The super positioned Cα–traces of RTA in complex with VHH F8 (green-cyan, respectively) and VHH G12 (gray-gray, respectively). The Cα–traces of (C) VHH F5 and (D) VHH F5. The VHHs are colored cyan with their CDR3 elements colored red. Key residues forming hydrophobic interactions are drawn as sticks and color coordinated to their respective main chain color.

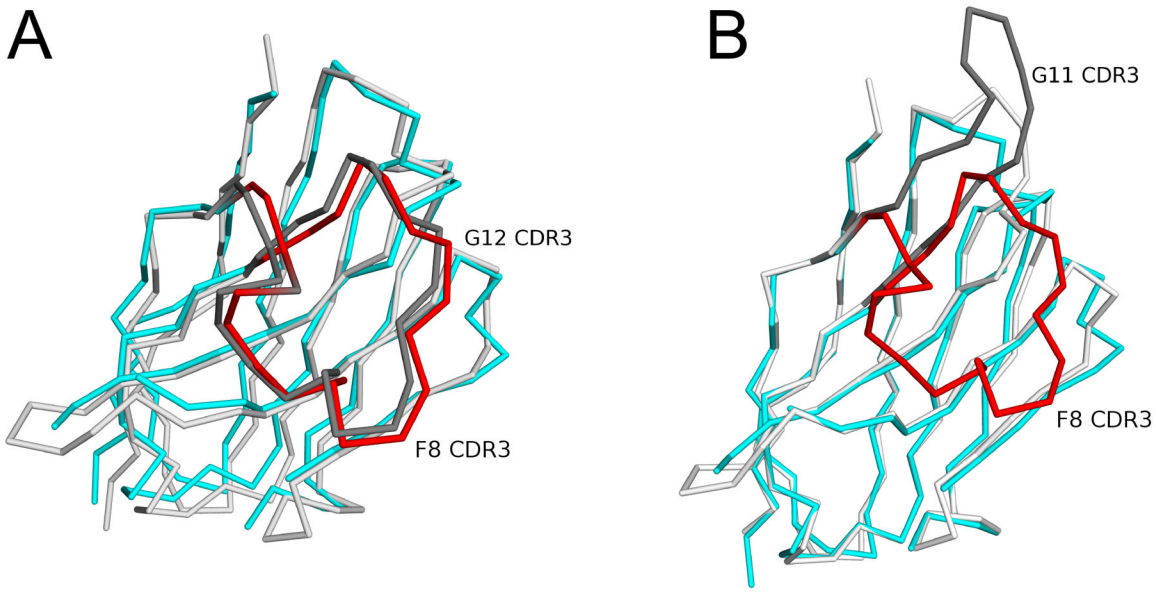

Figure 9. CDR3 conformations of VHH F8 relative to VHH G12 and VHH G11

Shown are the super positioned Cα–traces of VHH F8 with (**A**) VHH G12 and (**B**) VHH G11. The CDR3 element in F8 is colored red, while CDR3 elements of VHHs G12 and G11 are colored dark gray.

Table 1

Summary of RTA-VHH structures

	RTA-VHH[a]	
Parameter	**F5**	**F8**
d_{min} (Å)	1.5	2.0
Space group	$C222_1$	$C222_1$
$R^b/R_{free}{}^c$ (%)	17.8 / 19.5	20.4 / 25.7
PDB code	4Z9K	5E1H

[a], all complexes formed by co-crystallization.

[b] $R = \Sigma \mid |F_O| - |F_C| \mid / \Sigma \mid |F_O| \mid$, where F_O and F_C denote observe and calculated structure factors, respectively.

[c] R_{free} was calculated using 5% of data excluded from refinement.

Proteins. Author manuscript; available in PMC 2017 August 01.

Table 2

Summary of RTA-VHH binding data and interface information

				H-bonds[c]		Buried Surface Area (Å^2)			
VHH	**Kd**[a]	**IC_{50}**[a]	**CDR3**[b]	**Total**	**CDR1/2/3**	**Total**	**α-helix B**	**β-strand H**	**α-helix D**
F5	2.2	2.5	16	9	4/1/4	1760	477	1013	122
E5	1.9	5	10	16	4/3/6	1755	472	892	140
F8	0.2	300	22	9	0/0/9	1103	31	838	97
G11	0.56	90	15	10	0/0/8	1280	-	890	140
G12	0.15	300	22	9	0/0/9	1100	(9)[d]	870	70
A7	4.4	--	22	6	0/0/6	1060	-	715	85

[a], $\times 10^{-9}$ M;

[b], amino acid length;

[c], H-bonds between RTA and VHH (total) and CDR1, CDR2 and CDR3, respectively;

[d] the parentheses indicate that BSA is minimal that difficult to discern